IOP Publishing | Institute of Physics and Engineering in Medicine Physics in Medicine & Biology

Phys. Med. Biol. **61** (2016) 5621–5638 doi:10.1088/0031-9155/61/15/5621

Thermoacoustic range verification using a clinical ultrasound array provides perfectly co-registered overlay of the Bragg peak onto an ultrasound image

S K Patch[1,3], M Kireeff Covo[2,4], A Jackson[2], Y M Qadadha[1], K S Campbell[2], R A Albright[2], P Bloemhard[2], A P Donoghue[2], C R Siero[2], T L Gimpel[2], S M Small[2], B F Ninemire[2], M B Johnson[2] and L Phair[2]

[1] Department of Physics, UW-Milwaukee, 3135 N. Maryland Ave., Milwaukee, WI 53211, USA

[2] 88-Inch Cyclotron, Lawrence Berkeley National Laboratory, MS 88, 1 Cyclotron Rd., Berkeley, CA 94720, USA

E-mail: patchs@uwm.edu

Received 7 December 2015, revised 11 May 2016
Accepted for publication 8 June 2016
Published 6 July 2016

Abstract

The potential of particle therapy due to focused dose deposition in the Bragg peak has not yet been fully realized due to inaccuracies in range verification. The purpose of this work was to correlate the Bragg peak location with target structure, by overlaying the location of the Bragg peak onto a standard ultrasound image. Pulsed delivery of 50 MeV protons was accomplished by a fast chopper installed between the ion source and the cyclotron inflector. The chopper limited the train of bunches so that 2 Gy were delivered in 2 μs. The ion pulse generated thermoacoustic pulses that were detected by a cardiac ultrasound array, which also produced a grayscale ultrasound image. A filtered backprojection algorithm focused the received signal to the Bragg peak location with perfect co-registration to the ultrasound images. Data was collected in a room temperature water bath and gelatin phantom with a cavity designed to mimic the intestine, in which gas pockets can displace the Bragg peak. Phantom experiments performed with the cavity both empty and filled with olive oil confirmed that displacement of the Bragg peak due to anatomical change could be detected. Thermoacoustic range measurements in the waterbath agreed with Monte Carlo simulation within 1.2 mm. In the phantom, thermoacoustic range estimates and first-order range estimates from CT images agreed to within 1.5 mm.

Corresponding authors for [3]thermoacoustics and [4]chopper engineering.

Keywords: thermoacoustic, ultrasound, proton therapy, range verification, online adaptive planning

(Some figures may appear in colour only in the online journal)

1. Introduction

Proton beams deliver maximal dose to tissue within a small region defined by the Bragg peak, whereas x-ray photon beams deliver an exponentially decaying dose along the beam path, dosing healthy tissue proximal and distal to the tumor. Proton therapy delivers less dose to proximal tissue, and spares distal tissue altogether. Evidence-based medicine supports the use of proton therapy in tumors near the base of the neck, spine, eye and in pediatric patients (ASTRO Payer Relations Subcommittee 2013). However, range verification otherwise limits clinical utility of proton therapy (Knopf and Lomax 2013). Abdominal therapy is particularly problematic due to gas pockets that move rapidly within the gastrointestinal tract. Short-lived positron (Dendooven *et al* 2015) and prompt gamma emissions (Min *et al* 2006, 2012, Verburg *et al* 2013, Cambraia Lopes *et al* 2015, Hueso-Gonzalez *et al* 2015, Polf *et al* 2015) can provide fast and real-time feedback, respectively. An automated method for correlating PET data to underlying anatomy in CT images (Frey *et al* 2014) is slow and precludes online adaptive planning. To our knowledge, the possibility of real-time correlation of anatomy with Bragg peak location has not yet been presented.

Range verification via thermoacoustic detection of the Bragg peak is a natural consequence of the conversion of deposited dose to mechanical pressure pulses. Treatment plans are quantified in terms of Grays, $1\,\mathrm{Gy} = 1\,\mathrm{J\,kg^{-1}}$ (Selman 2000), whereas acoustic pulse amplitudes are quantified by Pascals, $1\,\mathrm{Pa} = 1\,\mathrm{N\,m^{-2}} = 1\,\mathrm{J\,m^{-3}}$. The units for dose and pressure differ only by a multiplicative factor of target density, ρ. The dimensionless Grüneisen (Γ) is simply the constant of proportionality between energy density and thermally induced pressure change. In other words, $\delta_p = \Gamma_\rho D$, where D is the dose delivered and δ_p is the induced pressure change.

Efforts to replicate thermoacoustic emissions due to rapidly evolving particle showers included pulsing ion beams from accelerators at Brookhaven National Laboratory (BNL) and the Institute for Theoretical Physics (ITEP). The BNL linac propagated 200 MeV protons in pulses as short as 3 μs (Sulak *et al* 1979), and the BNL fast extraction beam propagated 1.5 μs pulses of 30 GeV protons (Hunter *et al* 1981). Shorter pulse durations of 100 ns and less were achieved at ITEP (Albul *et al* 2005). Applicability to proton range verification was suggested by Tada *et al* who used the High Energy Accelerator Research Organization (KEK) synchrotron to propagate 50 ns pulses, each depositing 0.4 cGy (Tada *et al* 1991). Hayakawa *et al* detected thermoacoustic emissions during treatment of a hepatic cancer patient (Hayakawa *et al* 1995) using a single hydrophone, which precluded direct correlation of the tumor position with the thermoacoustic data. The beam fast extraction obtained at BNL, ITEP, and KEK facilities was performed with the particles at high energy, so it required kicker magnets to bend the beam. The magnets were pulsed with high voltage power modulators that utilized pulse forming networks designed for a fixed pulse length and frequency. Tandem electrostatic accelerators were also used to produce short ion beam pulses (Rohrer *et al* 1984), nevertheless they are limited by the maximum attainable voltage, confining the proton energy to few tens of MeV (Panofsky 1997). The chopping scheme of this paper was performed by an electrostatic chopper with the beam at lower energy, i.e. before the beam was accelerated by the 88-inch cyclotron. Consequently, the chopper plates required much lower voltage, increasing the reliability of the system, and could be switched with variable pulse lengths and frequencies, controlling the amount of energy deposited in the targets.

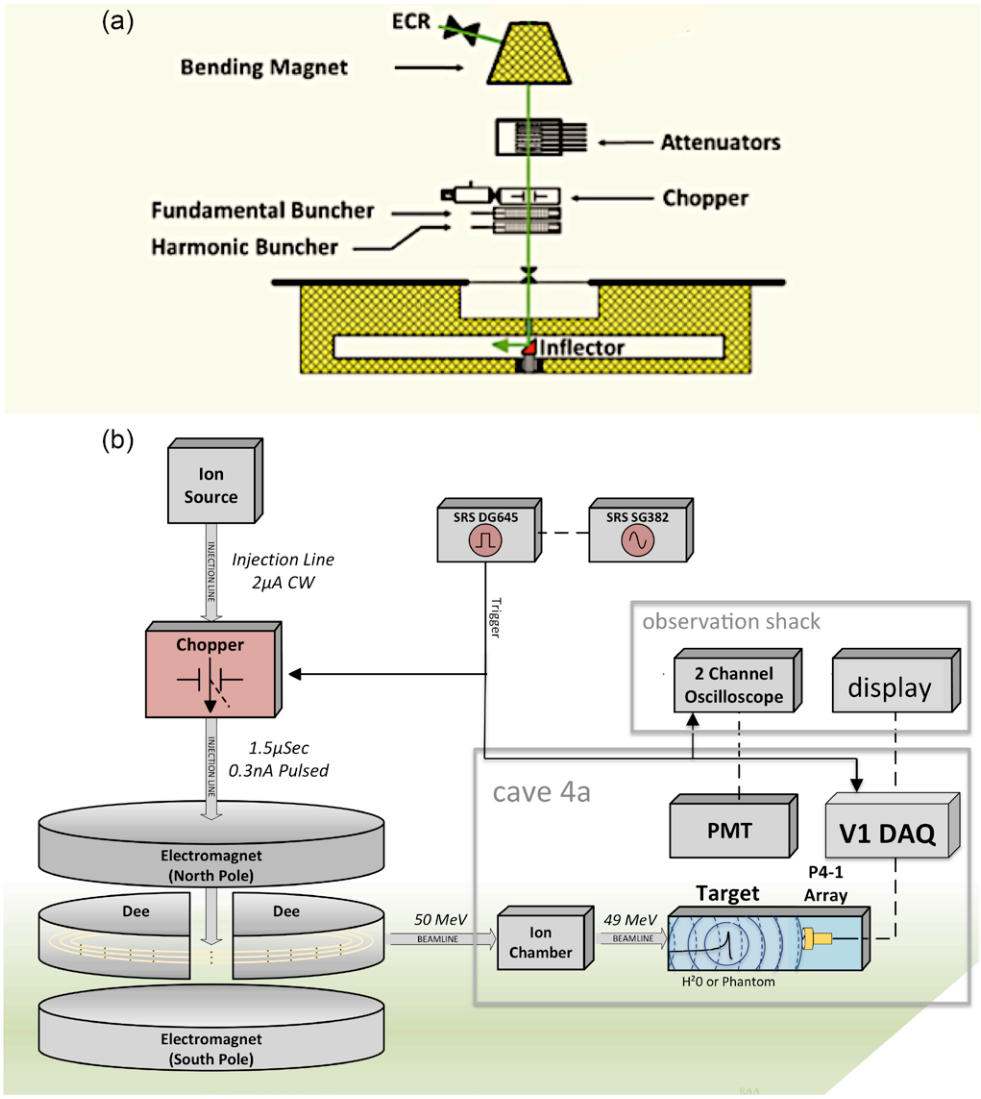

Figure 1. (a) Layout of the axial injection line, including fast chopper and electron cyclotron resonance (ECR) ion source. (b) Setup for thermoacoustic data collection. Trigger and measurement signals carried along solid and dashed black lines, respectively. Proton path indicated by thick grey arrows. Thin grey lines enclose experimental cave and observation shack. 'PMT' represents the photomultiplier tube.

The recent proliferation of proton therapy centers has spurred a renewed interest in thermoacoustic range verification. Measurements by individual receivers with lateral (Jones *et al* 2014) and distal (Ahmad *et al* 2015) offsets from the Bragg peak were simulated with an eye towards range verification. A mathematically complete set of measurements including both lateral and distal offsets was simulated to demonstrate feasibility of quantitative reconstruction of the dose deposition (Alsanea *et al* 2015). Recently, thermoacoustic emissions from 20 MeV pulses as short as 8 ns duration from a tandem electrostatic accelerator and 18 μs pulses of 220 MeV protons from the IBA C230 into water baths have been detected using

single element piezoelectric transducers (Assmann *et al* 2015) and a hydrophone (Jones *et al* 2015), respectively. The recent review (Polf and Parodi 2015) expands upon this brief summary.

We present experimental improvements to proton delivery, acoustic detection, and image display. An injection line chopper (figure 1(a)) truncated 2 μA beams of 50 MeV protons into pulse durations of less than 2 μs full width at half maximum (FWHM) delivering 2 Gy in a single pulse. Unlike previous results in which thermoacoustic emissions were detected by single-element transducers or hydrophones without online correlation to anatomy, we acquired with a *clinical ultrasound array.* Standard ultrasound images were acquired using the same transducer array, enabling perfectly co-registered color overlay of the Bragg peak location and also the beam's entry point into the target.

2. Theoretical background

Thermoacoustic emissions from a proton beam aligned with the z-axis propagate according to the inhomogeneous linear acoustic wave equation,

$$\left[\frac{\partial^2}{\partial t^2} - \nu_s^2 \Delta\right] p(\mathbf{x}, t) = \Gamma / \mathrm{Q}\ \mathrm{d}(\mathbf{x})\ I'(t) \tag{1}$$

where $\mathbf{x} = (x, y, z)$, zero initial conditions are assumed, soundspeed is represented by ν_s, $I(t)$ is the beam current in Amperes, and $Q = \int_0^T I(t) dt$ is the charge delivered during a pulse period of T seconds. Energy density due to a single pulse is given by $d(\mathbf{x}) = D(\mathbf{x})\rho(\mathbf{x})$ where ρ is density D and is dose delivered in Gy, distributed according to $D(\mathbf{x}) = (4\pi\sigma^2)^{-1} \exp[-(x^2 + y^2)/(4\sigma^2)]\ s(\mathbf{x})\ (Q/E)$ where $s(\mathbf{x})$ is the per proton stopping power in MeV m^2/kg and e is the fundamental charge.

Assuming constant soundspeed and Grüneisen, solutions to equation (1) can be written in terms of spherical means of the product of energy density, d, times the Grüneisen (John 1981),

$$p(\mathbf{x}, t) = Q^{-1} I * \frac{\partial}{\partial t} \{t M[\Gamma d](\mathbf{x}, \nu_s\ t)\} \tag{2}$$

where $M\ [\Gamma d]\ (\mathbf{x}, \nu_s\ t)$ is the mean value of $\Gamma\ d$ on the surface of a sphere of radius $\nu_s\ t$ centered at transducer location $\mathbf{x}$, and convolution is carried out with respect to time over the interval $(0,\ t)$. Although $M\ [\Gamma d]$ and I are both non-negative, the time derivative results in both positive and negative pressures, corresponding to compression and rarefaction, respectively.

Instantaneous delivery ($I = \delta$) would correspond to idealized thermoacoustic emissions $\frac{\partial}{\partial t}\{t\ M[\Gamma d](\mathbf{x}, \nu_s\ t)\}$ but measurements by a perfect point receiver would be bandlimited by transducer location, $\mathbf{x}$, the Grüneisen, $\Gamma(\mathbf{x})$, and energy deposition, $d(\mathbf{x})$, which is determined by beam properties (energy and width) as well as target stopping power. In practice, beam is delivered by a non-impulsive current, $I(t)$, which also bandlimits thermoacoustic emissions. Frequency response of the receiver further bandlimits measured data.

3. Methods and materials

The experiment was conducted at the 88″ Cyclotron at Lawrence Berkeley National Laboratory, which is a sector-focused cyclotron with energy constant K of 140. The cyclotron can provide different ion species and charge states for energy variable experiments to a maximum energy

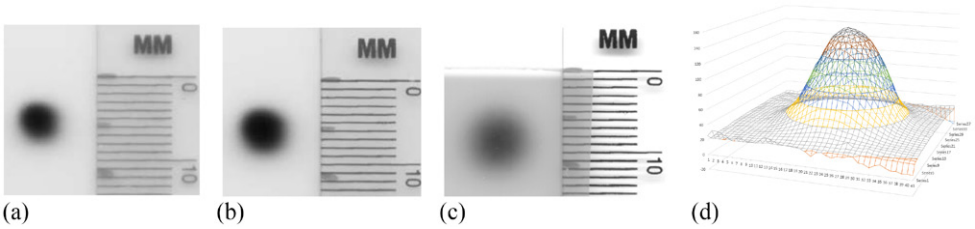

Figure 2. Overexposed Gafchromic films taken in water bath at distances of 4 mm (a) and 18 mm (b) from tank wall. Lightly exposed film taken inside cavity of phantom (c) and 3D mesh showing Gaussian beam shape (d).

of 55 MeV u^{-1} (Covo 2014). The cyclotron was tuned to produce 50 MeV of proton beam and thermoacoustic emissions were collected during a 28 h shift. Trigger validation and proton pulse shape were measured during a subsequent run on the same cyclotron. A fast scintillator was used to measure the delay between the trigger and the ion beam arriving to the target. A clinical ultrasound transducer array detected thermoacoustic emissions from locations on the beamline distal to the Bragg peak, as indicated in figure 1(b). Elements which were customized for this research are described in detail below.

3.1. Beamline and chopper

A 50 MeV beam with 2 μA current exited the cyclotron and entered an ion chamber, losing approximately 1 MeV before entering the target (water bath or gelatin phantom). The beam was focused to 4 mm diameter upon entrance into the target, as confirmed by Gafchromic film in figure 2(a).

An injection line chopper deflected the beam as it passed between parallel plates, allowing protons to pass to the cyclotron only when the plates were discharged. There is no dosimetric consequence by deflecting the beam at the injection line, before it is accelerated by the cyclotron, because the beam is at low energy, i.e. less than 25 keV u^{-1}.

The chopper uses a fast square wave pulser (Behlke, model FSWP-51-02) that can provide ± 1 kV and is connected to two parallel electrostatic deflector plates, which are 6″ wide and 3.25″ long with a separation of 3.25″. Results below were generated by a pulsewidth on the injection line of 1.5 μs, which delivered $2\,\mu\text{A} \times 49\,\text{MeV} \times 1.5\,\mu\,\text{s} = 147\,\mu\text{J}$ to the target. As detailed in section 3.4.1, approximately 2 Gy were delivered within the Bragg peak per pulse, inducing pressure jumps of $200\,\text{Pa} = 0.1^{*}\,1000\,\text{kg m}^{-3}{}^{*}2\,\text{J kg}^{-1}$. Proton pulses were delivered at a repetition frequency of 100 Hz.

The pulsers are formed by series-connected power metal oxide semiconductor field-effect transistors (MOSFETs) which are triggered synchronously by a galvanically isolated driver control circuit. The unit has a floating configuration, so it can produce positive or negative pulses by grounding the positive or negative end of the push–pull arrangement. To match the impedance and to protect the switches, series resistors are built in. Internal ceramic capacitors ensure adequate buffering of the external high voltage supply. The pulser has direct liquid cooling that uses a dielectric liquid with excellent specific heat capacity and insulation, so it can continuously switch at 3 MHz with a maximum power dissipation of 1500 W. The pulser is protected against overheating due to rapid frequency switching by a thermal interlock that disables the control circuit when the temperature exceeds 75 °C.

The chopper is followed by fundamental and harmonic gridded bunchers that compress the ions longitudinally into buckets that are adjusted to the phase acceptance of the cyclotron.

Nevertheless, the 1.5 μs injection line pulsewidth spread to a delivered pulse envelope, $I(t)$, with full-width at half-maximum (FWHM) of 1.76 μs, which was measured by a fast scintillator and photomultiplier tube assembly located approximately one foot from the target.

Ultrasound acquisition and chopper were triggered by a signal from a SRS DG645 digital delay generator that is synchronized to the SRS SG382 signal generator, which provides the RF reference signal for the cyclotron, with a rubidium timebase. The fast scintillator was used to measure the delay between the trigger and the ion beam arriving to the target.

3.2. Ultrasound hardware

Thermoacoustic emissions were measured by a programmable ultrasound system (Verasonics V1) with a 96-channel P4-1 cardiac array (ATL). The P4-1 array was selected because it was the lowest frequency imaging array compatible with the Verasonics V1 system. The P4-1 array is marketed as sensitive over the 1–4 MHz frequency band. However, it is important to note that manufacturers' ultrasound transducer specifications are ill-suited to quantitative thermoacoustic imaging. Hydrophone manufacturers typically provide a digital file with frequency response in receive-only mode. Single element transducers like those used by Assmann *et al*, are accompanied by a sheet of paper from Olympus on which pulse-echo frequency response is plotted, assuming a particular pulser-receiver. Although reciprocity of the piezoelectric transducer in transmit and receive modes is a good assumption, the transmit and receive electronics are different. The aggregate transmit-receive frequency response provided by the manufacturer does not represent the receive-only response of the transducer connected to a low-noise preamplifier. The situation for clinical ultrasound arrays is even worse, as manufacturers do not often provide the aggregate Tx/Rx frequency response. Receive-only response of the ATL P4-1 transducer attached to the Verasonics V1 electronics has not been quantified, but this combination has demonstrated sufficient receive sensitivity in the 100 kHz–4 MHz band to capture broadband thermoacoustic emissions from surgical tissue specimens (Patch *et al* 2015). The array had a 300 μm element pitch, and an active surface with length 2.8 cm in lateral direction. The V1 system electronics sampled at 30 MHz and amplified by 43.5 dB.

3.3. Data processing

Thermoacoustic image reconstruction typically refers to reconstructing the idealized initial pressure, or more accurately, $[\Gamma d]\,(\mathbf{x})$, throughout the field of view from pressures measured at transducer locations outside the field of view. Reconstruction can be performed by time-reversal, harmonic expansions, or filtered backprojection, and each approach has generated references too numerous to cite. Idealized data measured over an aperture surrounding the region of interest can be inverted exactly. In practice, however, measurements are bandlimited, noisy and incomplete. Fortunately, range verification of a monoenergetic beam with well-defined Bragg peak does not require mathematically exact reconstruction of the energy density, $d(\mathbf{x})$.

Data was reconstructed by filtered backprojection. A lowpass filter with kernel identically one from DC to 700 kHz and smoothly transitioning to zero over the interval (700 kHz, 800 kHz) was applied in software, but it is important to note that piezoelectric ultrasound transducers apply high-pass bandlimits as well. Additionally, each time series was Hilbert transformed prior to backprojection into the plane defined by the transducer.

Backprojection is sometimes referred to as 'one-way' or 'receive-only' beamforming. To simplify color overlay of the Bragg peak, phantom data was backprojected onto the same

pixel locations as in ultrasound images. Axial discretization was $\Delta z = 296\,\mu$m, to depths of 34.9 mm and 118.4 mm in water and phantom, respectively. Lateral discretization was $\Delta x = 283.5\,\mu$m in the waterbath, and $\Delta x = 567\,\mu$m in the phantom. Fields of view ranged laterally over $\pm$ 19.1 mm and $\pm$ 75.7 mm in the waterbath and phantom, respectively.

The reconstructed image is a heavily filtered version of $[\Gamma d]$ (**x**), isotropically high-passed by ultrasound hardware and low-passed by I. Anisotropic filtering of 'wave-fronts' due to limited angular coverage increases with distance from the transducer array. Limited angle streak artifacts running nearly parallel to the face of the transducer array therefore increase with image depth, as angular coverage decreases. Images should be non-negative, but are not because very low frequencies, including DC, are suppressed.

Thresholds were applied to select regions of strong positive pressure, representing the Bragg peak, and low pressure, representing the point at which the beam entered the target. A threshold of 80% of the maximum and minimum values was applied to select pixels near the Bragg peak and beam entry point into the target. Coordinates of selected pixels were then averaged to robustly determine the Bragg peak and entry point locations.

3.4. Targets

Two targets were utilized. A water bath provided a homogeneous and characterizable target with low acoustic attenuation. A gelatin phantom designed to match the nominal soft tissue properties for ultrasound imaging was fabricated with a cavity to mimic the intestine. Range estimation was performed with the intestinal cavity both empty and full of olive oil to demonstrate feasibility of detecting anatomic change due to digestion. Following Sulak *et al*, a Styrofoam cone was embedded in the gelatin phantom to ensure that 50 MeV protons traveled into the center of the phantom. Each target was positioned approximately 10 cm distal from an ionization chamber. Distances along the beamline through materials that were proximal to the Bragg peak are provided in table 1. X-ray CT scans of the phantom and sidewall of the waterbath yielded Hounsfield units (HU) on the standard CT scale. Using HU as proxy for density yields a first order estimate of relative stopping power, $\rho_s = \rho/1000$. Table 1 also contains thermoacoustic properties: soundspeed (ν_s), acoustic impedance (Z) and the dimensionless Grüneisen (Γ) for relevant materials.

Thermoacoustics relies upon rapid heating, and it is important to control that heating because the Grüneisen and soundspeed are temperature dependent. Although individual proton tracks experience superheating (Learned 1979, Toulemonde *et al* 2009), dissipation occurs quickly so that average temperatures and induced pressures within the target volume remain low. Upper bounds for heating rates averaged throughout the targets and within the Bragg peak are computed using the formulae $r_{\text{ave}} = \frac{150\,\mu\text{J} \times 100\,\text{Hz}}{m \times C}$ and $r_{\text{peak}} = \frac{2\,\text{Gy} \times 100\,\text{Hz}}{C}$, respectively, where m is target mass and C represents specific heat capacity. The final column in table 2 lists the temperature rise per Gy for comparison.

3.4.1. Monte Carlo simulations of thermoacoustic emissions in waterbath. Testing was performed in a large water bath, contained in a 112-quart storage container (HOMZ) filled with low conductivity water. To confirm the beam geometry Gafchromic films were suspended in the waterbath perpendicular to the beamline. A tight focus of 4 mm diameter at the point of entry (a) increased to 6 mm diameter at a depth of $z = 18$ mm (b).

A SRIM simulation tracked 30 000 protons with 49 MeV energy incident upon a two-layer target. SRIM is a Monte Carlo program that calculates the stopping and range of ions in matter using a quantum mechanical treatment of ion-atom Coulomb collisions (Ziegler *et al* 2010).

Table 1. Material properties.

Material	d (mm)	HU	ρ_s	ν_s (m s^{-1})	Γ	Z (Mrayls)
Air	100	-998.8 ± 2.9	1.2×10^{-3}	340	NA	4×10^{-4}~ 0
Styrofoam cone	135	-966.1 ± 9.5	0.034	~340	NA	~10
Gel-infused Styrofoam	3	-784.0 ± 157.5	0.216	<1540	NA	<300
LDPE tank wall	2	-222.6 ± 39.5	0.777	1950	1.14	1.52
Olive oil		NA	0.911	1430	0.73	1.30
Gelatin phantom		-2.4 ± 4.4	0.998	1540[a]	0.23[b]	1.54
Water		0.6 ± 3.3	1	1480	0.11	1.48

Two properties of the phantom material were estimated.
[a] The nominal soundspeed used in ultrasound is assumed for this phantom which has low oil content and is similar to phantoms characterized in (Madsen *et al* 1982).
[b] A weighted average of the Grüneisen's of water and oil was assumed.

Table 2. Heating rates.

Material	m (kg)	C (kJ kg^{-1} K^{-1})	r_{ave} (K s^{-1})	r_{peak} (K s^{-1})	ΔT / Gy(mK)
Water	100	4.2	36×10^{-9}	0.05	0.24
Olive oil	0.1	1.8	83×10^{-6}	0.11	0.56
Gelatin phantom	4	4	1×10^{-6}	0.05	0.25

It considers the velocity dependent charge state of the ion and the long range screening interactions, which can create electron excitations and plasmons within the target. SRIM follows each ion collision and all target atom cascades, providing details of ion distribution, target damage, sputtering, ionization, and phonon production.

The first layer was modeled as 2 mm low density polyethylene (LDPE), representing the tank sidewall, followed by water in the second layer. Stopping power was reported along the beamline in 250 μm increments and predicted the Bragg peak to occur at 21.1 mm from the tank outer wall, or 19.1 mm inside the water. The beam was assumed to have a Gaussian radial profile with $\sigma = 2$ mm. From this spatial distribution of the dose deposition and knowledge that 0.147 mJ were delivered we computed the dose deposited per pulse, $D(\mathbf{x})$, with 2.0 Gy delivered at the Bragg peak (figure 3(a)). The delivered beam current, $I(t)$, had FWHM of 1.76 μs, as plotted in figure 3(b).

Multiplying dose by density and the Grüneisen yields initial pressure assuming instantaneous delivery. Instantaneous initial pressure exceeded 200 Pa in the Bragg peak and also in the LDPE, as shown by the gray scale image in figure 3(c), which has the same aspect ratio as figure 3(a). Although dose in the LDPE sidewall was comparable to that in the nearby water, the induced initial pressure was high in the LDPE because the Grüneisen of LDPE is greater than that of water.

Evaluating equation (2) at the point on the beamline 6.5 mm distal to the Bragg peak models a thermoacoustic pulse induced by a spill delivering current $I(t)$. Thermoacoustic emissions due to idealized instantaneous and experimentally realized spills are modeled in figure 3(c) by thin and thick yellow lines, respectively. Dashed green lines represent spherical surfaces over which the non-negative source term, Γd, is integrated to provide $M[\Gamma d](\mathbf{x}, \upsilon_s t)$. The strong spatial gradient in Γd combined with the time derivative in $\frac{\partial}{\partial t}\{t\, M[\Gamma d](\mathbf{x}, \upsilon_s t)\}$ lead to sharp bipolar pulses emanating from the LDPE. If the Grüneisen of LDPE matched that of water,

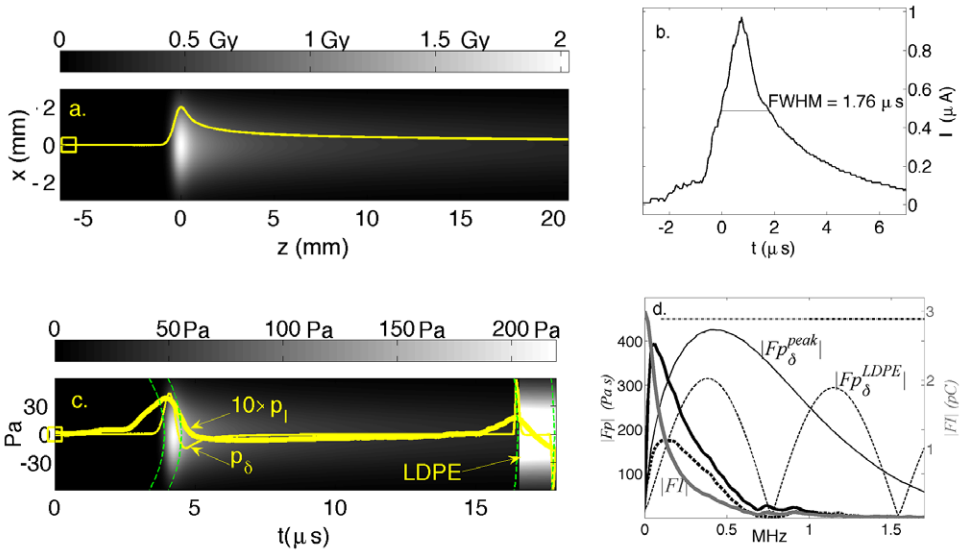

Figure 3. Pulses in waterbath. (a) SRIM model of dose along beam axis plotted in yellow, overlaid on a cross-sectional image assuming $\sigma = 2$ mm. (b) Measured envelope of delivered proton current, I. (c) Initial pressure due to instantaneous spill modeled in the gray scale image. Dashed green lines represent spherical integration surfaces used to evaluate equation (3). Thermoacoustic emissions arriving at the distal location indicated by a square yellow box are plotted in yellow. Emissions from instantaneous (p_δ) and experimental (p_I) spills are plotted in thin and thick yellow lines, respectively. (d) Spectra and the transducer's sensitivity bands. Spectra corresponding to emissions from water and LDPE plotted separately. Idealized spectra from impulsive beam delivery in thin lines; $|\mathbf{F}I|$ and the bandlimited spectra plotted in thick grey and black, respectively. Horizontal dashed-dot lines represent regions of P4-1 sensitivity bands. Black is within the 3 dB region, grey lies below.

the pulse emanating from the tank wall would be a negative monopole, reduced in amplitude because the Grüneisen of water is lower than that of LDPE. Numerical integration over the sphere was performed using Gaussian quadrature over the $\theta \in [0, \pi]$ interval and the trapezoidal rule for $\phi \in [0, 2\pi]$ in the detailed representation of equation (2):

$$p(\mathbf{x}, t) = I * \frac{\partial}{\partial t}\left\{ \frac{1}{4\pi \upsilon_s^2 t} \int_{\phi=0}^{2\pi} \int_{\theta=0}^{\pi} [\Gamma d](\mathbf{x} + \upsilon_s\, t\mathbf{u}(\theta, \phi)) \mathrm{d}\theta \mathrm{d}\phi \right\} \tag{3}$$

where $\mathbf{u}(\theta, \phi) = (\cos\phi \sin\theta, \sin\phi \sin\theta, \cos\theta)$ is the standard unit vector on the surface of a sphere. Differentiation and convolution with respect to time were implemented in the Fourier domain. To analyse the impact of the current pulsewidth, subscripts will denote the beam current. p_δ denotes impulsive delivery, whereas p_I denotes of pulsed current $I(t)$.

Although initial pressures exceed 200 Pa in the Bragg peak and LDPE, $p_\delta(\mathbf{x}, t)$ remains below 50 Pa at the distal transducer location $\mathbf{x}$= (0, 0, 6.5 mm) as the thermoacoustic pulse travels past. The experimentally realized pressure, $p_I(\mathbf{x}, t)$, is reduced by approximately one order of magnitude, due to convolution by the delivered current, $I(t)$, which is plotted in figure 3(b). p_I is compared to p_δ and the initial pressure in figure 3(c).

Spectra of thermoacoustic emissions and the sensitivity band of the P4-1 transducer are shown in figure 3(d). $|\mathbf{F}I|$, the magnitude of the current spectrum is plotted in thick grey,

Table 3. Phantom constituents by % mass.

Water	Kerosene	Safflower oil	200-bloom gelatin	n-propanol	Surfactant	Formaldehyde	p-toluic acid
67.3	7.2	8.2	12.1	3.5	0.9	0.8	0.1

whereas spectra of thermoacoustic emissions bandlimited by I are plotted in thick black. Idealized pulses due to instantaneous delivery are plotted with thin lines. Clinically relevant spectra from the Bragg peak and the potentially confounding spectra from the LDPE are plotted separately in solid and dashed lines, respectively. The spectrum of a pulse generated instantaneously by the LDPE sidewall, $\mathbf{F}p_\delta^{\mathrm{LDPE}}$, decays slowly, whereas the ideal spectrum generated by the Bragg peak, $\mathbf{F}p_\delta^{\mathrm{peak}}$, achieves its maximum below 500 kHz and has full-width at half-maximum of 1 MHz. Bandwidths of the experimentally realized pulses are reduced to 700 kHz, as plotted in thick lines. The marketed 1–4 MHz sensitivity band is indicated with a black dashed horizontal line, whereas the 100 kHz–1 MHz region containing most of the signal energy is indicated by a grey dashed horizontal line.

3.4.2. Gelatin phantom with intestinal cavity. Phantoms were fabricated following the procedure outlined in (Lazebnik *et al* 2005), with contents by weight listed in table 3. A 'U-shaped' cavity designed to mimic an intestine was located at the end of a 135 mm long Styrofoam cone, as seen in figure 4. The cavity had ellipsoidal cross-section (26 mm and 36 mm primary axes). Lightly exposed Gafchromic film placed inside the cavity confirmed the beam traveled through the Styrofoam cone and into the center of the cavity, and had a Gaussian profile, as shown in figures 2(c) and (d). When full of olive oil, the beam stopped midway through the oil, indicated by the solid arrow in figure 4(c). When empty, the beam traveled through the air-filled cavity before stopping in the phantom, as indicated by the dashed arrow.

Acoustic attenuation of thermoacoustic emissions was low. Attenuation in similar gelatin phantoms has been modeled as αf^b, where f represents frequency in MHz. Conservative estimates for the constants are $\alpha = 1\,\mathrm{dB\,cm^{-1}MHz^{-b}}$ and $b = 1.1$ (Madsen *et al* 1982). As shown in figure 3(d) thermoacoustic emissions were bandlimited below 700 kHz, implying a maximum attenuation of 0.68 dB cm^{-1}. However, the spectrum of the experimentally realized thermoacoustic emission from the Bragg peak achieves its maximum near 100 kHz, where acoustic attenuation is only 0.08 dB cm^{-1}.

3.5. Water tank experiment

Care was taken to minimize acoustic reflections. The tank was filled to approximately 40 cm height, matching the width of the tank. It was positioned so that the beam entered horizontally at a height of approximately 20 cm, so that acoustic propagation time from Bragg peak to the left and right sidewalls, bottom and air–water interface was at least 120 μs. However, two-way propagation time from Bragg-peak to the entry sidewall and back was 28 μs.

Thermal stability during the 40 min acquisition window was controlled primarily by the large volume of water used. The tank was filled the evening prior to data acquisition, to ensure the water stabilized to room temperature. Table 2 provides an upper limit of 0.5 K temperature increase in the Bragg peak during a 10 s acquisition of 1024 pulses. The beam was pulsed throughout most of the 40 min acquisition window, implying an upper limit of 120 K temperature increase in the Bragg peak, but this is a gross overestimate neglecting both thermal diffusion and natural convection. Diffusion alone would not suffice to maintain room temperature

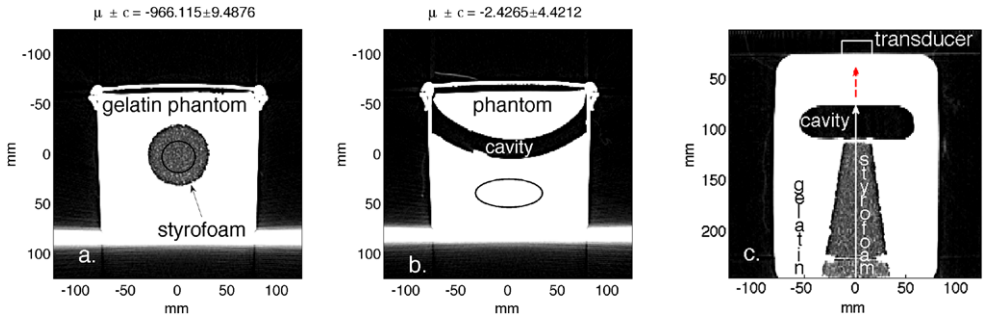

Figure 4. CT scans of phantom shown with display window (−1000, −900) HU. Ellipses indicate regions over which HU values were averaged for table 1. (a) Axial slice through styrofoam cone. (b) Axial slice through air-filled cavity. (c) Coronal slice in which beam traveled through styrofoam cone and cavity.

but natural convection served to mix the water and maintain thermal stability. Thermoacoustic emissions were reconstructed assuming the soundspeed of 20° C water, 1480 m s^{-1}.

The ultrasound array was positioned in the waterbath distal to the Bragg peak. To protect the electronics in the clinical array's handle from water damage, a thin plastic bag provided a water-tight barrier. Acoustic coupling gel (Aquasonic) between the transducer and bag ensured good acoustic transmission. The transducer array was manually positioned along the *z*-axis, but stepper motors were used to position in the *x*-*y* plane. The array was aligned to the beam line axis with an optical alignment tool that is located inside the cave (Johnson *et al* 2006). The ultrasound array was initially centered on the beamline, 6.5 mm distal to the Bragg peak, with horizontal lateral orientation as if it were detecting a coronal image. Thermoacoustic pulses were then detected at three lateral locations, centered along the beamline and also translated left and right by 10 mm.

3.6. Gelatin phantom experiment

Data was again collected with the transducer array located on the beamline, distal to the Bragg peak. Ultrasonic gel was applied to the P4-1 array to achieve acoustic coupling. B-mode imaging was performed first to ensure the P4-1 transducer was located along the beamline, and raw ultrasound data was saved to disk in order to perfectly co-register ultrasound and thermoacoustic images. Without moving the P4-1 array, 1024 thermoacoustic pulses were averaged on the Verasonics' host computer and saved to disk. Two sets of thermoacoustic emissions were recorded, one with the cavity empty and another with the cavity filled with olive oil. Acoustic propagation speed was assumed to be 1540 m s^{-1} for both ultrasound and thermoacoustic imaging (Madsen *et al* 1982).

Care was taken to minimize heating in the phantom, and the pulsed beam was delivered for only 5 min per phantom experiment. During a 10 s acquisition table 2 implies upper limits on Bragg peak heating of 1.1 K and 0.5 K in the olive oil and gelatin phantom, respectively. During the five-minute acquisition windows these estimates become 33 K and 15 K, enough to affect the Grüneisen and soundspeed. Although more viscous than water, convection likely occurred in the olive oil, as no temperature increase was noted when the oil was removed after each 'cavity full' measurement. However, diffusion was the only mechanism providing thermal stability in the solid gelatin phantom. 15–30 min of positioning time between experiments allowed for some thermal stabilization.

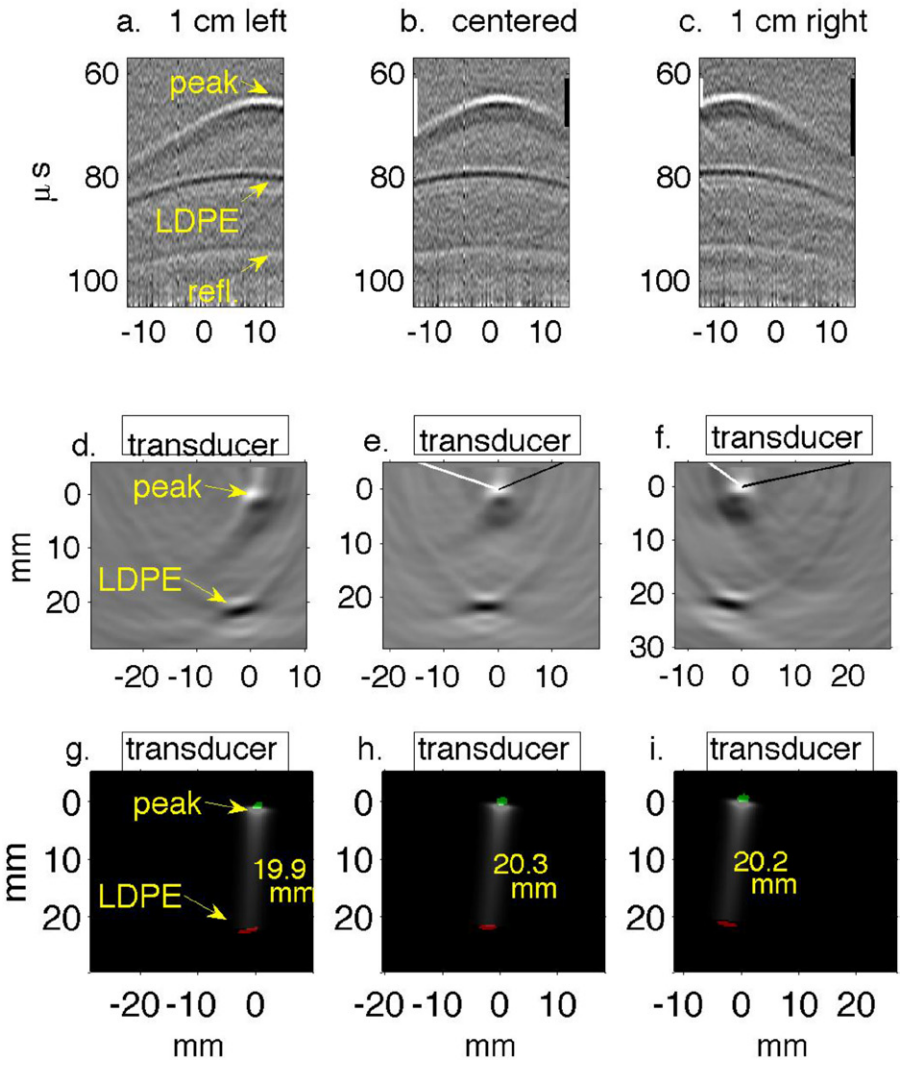

Figure 5. Water tank results in which transducer is translated in 1 cm increments perpendicular to the beamline. In figures (a), (d) and (g) the transducer axis is 1 cm left of the beamline. In figures (b), (e) and (h) the transducer is centered on the beamline, and in figures (c), (f) and (i) it is 1 cm right of the beamline. (a)–(c) Filtered P4-1 data, with timing measured from chopper plate discharge, not entry of beam into target. Horizontal axes represent channel number. (d)–(f) Reconstructions of the data reveal the Bragg peak as a monopole 6.5 mm from the transducer. The proximal end of the beam as it enters the LDPE appears as a bipolar mark. (g)–(i) Regions of strongest and weakest pressures from (d) to (f) overlaid onto Monte Carlo simulations in green and red, representing Bragg peak and LDPE, respectively.

4. Results

Signal averaging was required to visualize the Bragg peak in the data as displayed in real-time on a computer monitor. In the interest of time, an overly conservative choice of 1024 proton pulses was made.

4.1. Water tank results

The pulse emanating from the Bragg peak was nearly spherical, and traveled outward in all directions. The part that traveled towards the entrance wall was reflected and returned to the transducer array. All three pulses, Bragg peak direct, LDPE direct and Bragg peak reflected, can be seen in figures 5(a)–(c), where readouts from all 96 transducer channels are displayed.

Acquisition of thermoacoustic emissions was triggered by the same signal as the chopper, which initiated proton acceleration. Only after protons were delivered to the target could subsequent thermoacoustic emissions travel to the transducer array. Because the transducer's 2.8 cm lateral width exceeded its axial distance from the Bragg peak by a factor of four, channels on the array closest to the Bragg peak detected signal sooner than those on either end, causing arc-shaped first arrivals in the data show in figures 5(a)–(c). White and black vertical lines in figures 5(b) and (c) represent delays between proton delivery and first arrival of the Bragg peak signal in channels 1 and 96 on either end of the transducer array. White and black lines in reconstructed images in figures 5(e) and (f) have length of the corresponding time delays multiplied by soundspeed. To determine the time at which protons were delivered to the target, reconstruction was performed over a range of delivery times. The Bragg peak and LDPE signals came into focus using $t_o = 61$ μs after the chopper plate discharge.

The P4-1 array was positioned about 1″ from tank wall, attached to a stepper motor that translated nearly parallel to vertical tank wall. Data was collected at three transducer positions: centered with respect to the Bragg peak, and translated right and left by 1 cm each. Shifted arcs in filtered data shown in figures 5(a)–(c) correspond to shifted Bragg peak locations reconstructed in figures 5(d)–(f) and overlaid onto Monte Carlo dose simulations in figures 5(g)–(i).

The Bragg peak is reconstructed as a round monopole in figures 5(d)–(f), whereas the LDPE tank wall appears as an oblong bipolar structure. The bipolar nature of the LDPE interface is due to its high thermal expansion coefficient. The front and back edges generated compressional and rarefaction pulses, respectively. Lateral smearing of the entry point into the LDPE is a limited angle reconstruction artifact. Angular coverage of the Bragg peak exceeded 120° (atan(14/6.5)), whereas coverage of the beam entry point was less than 60° (atan(14/26.5)).

Relative amplitudes of the Bragg peak and LDPE pulses agree qualitatively with back-of-the-envelope calculations that account for differences in dose deposition, Grüneisen, and distance to the transducer element. The 49 MeV beam deposits into the LDPE only 1/6 of the dose at the Bragg peak, but the Grüneisen is an order of magnitude higher in LDPE than water. Therefore, the initial pressure jump in the LDPE is a factor of 1.7 greater than in the Bragg peak. Acoustic attenuation is negligible in water, but geometric spreading of the nearly spherical acoustic pulses emanating from Bragg peak and the point of entry on the LDPE reduce their amplitudes by factors of 1/6.5 and $1/26.5 = 1/(6.5 + 20)$, respectively. Therefore, pulses from the Bragg peak should be two times stronger than those from the LDPE front wall. In figure 5 the ratios range from 1.6 to 1.9.

Using local maxima and minima in the images figures 5(d)–(f) to quantify distance between the points of maximal dose in the Bragg peak and the minimum in the air-LDPE interface consistently underestimates the 21.1 mm range with results from 19.9 mm to 20.3 mm, as shown in figures 5(d)–(f) and overlaid in figures 5(g)–(i).

4.2. Phantom results

Images in figure 6 show translation of the Bragg peak due to air in the intestinal cavity and highlight the difficulty of using ultrasound imaging alone for range verification. Filtered time

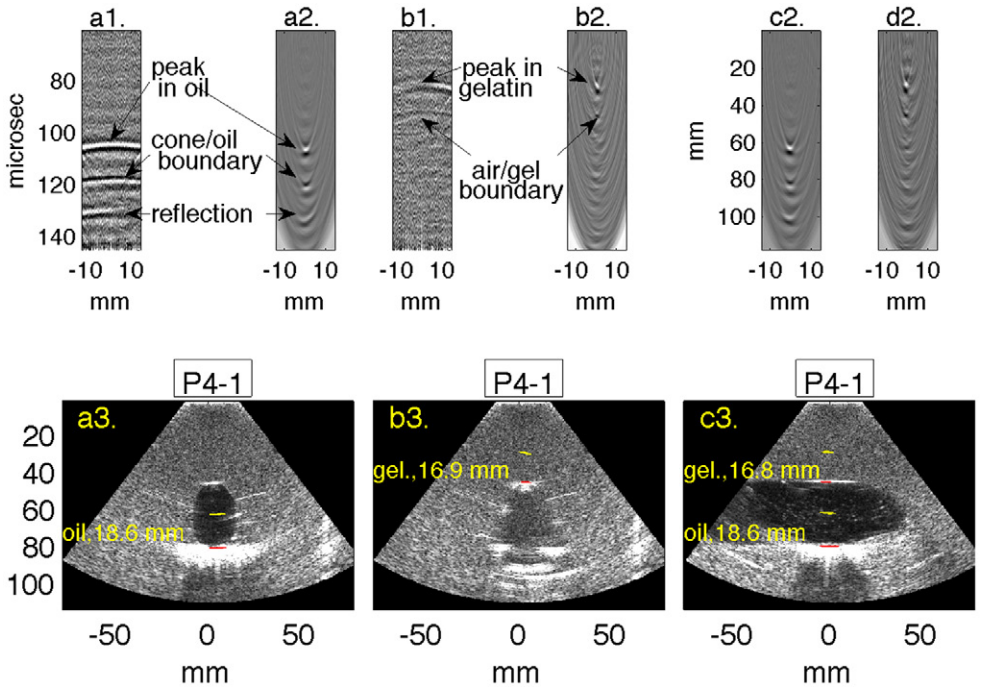

Figure 6. Time series, reconstructions and overlays onto grayscale ultrasound images. Subfigures are labeled with letters corresponding to transducer orientation and cavity status, and numbers indicate data type. (a) Sagittal, cavity filled with olive oil. (b) Sagittal, cavity empty. (c) Coronal, cavity filled with olive oil. (d) Coronal, cavity empty. (1) Filtered thermoacoustic time series, (2) reconstructed thermoacoustic image, (3) grayscale ultrasound image with Bragg peak overlaid in yellow; beam entry point into high stopping power target in red. Overlays from both empty and filled cavity are shown in (c3).

series and reconstructed thermoacoustic images are shown above grayscale ultrasound images with overlays of Bragg peak location in yellow and beam entry point in red. Sagittal images with the cavity filled with olive oil and empty are shown in the 'a' and 'b' subfigures, respectively. Thermoacoustic images from both empty and filled cavity are overlaid onto the coronal ultrasound image in subfigure 'c'. The oil-filled cavity in figure 6(a3) appears as an anechoic dark region, but reflection of ultrasound at an air/tissue interface in figure 6(b3) makes the speckle pattern inside the cavity similar to that of the surrounding phantom material.

Although the transducer-to-Bragg peak distance doubles when the cavity is filled with olive oil, SNR increases because the thermal expansion coefficient of olive oil (figure 6(a1)) is higher than that of the gelatin phantom (figure 6(b1)). Additionally, the late-arriving signal from olive oil displays a weaker curvature than that from the gelatin, because the transducer to Bragg peak distance is nearly doubled when the cavity is filled with olive oil.

Thermoacoustic range estimation was again performed by averaging locations of pixels at which the reconstructed images exceeded the 80% threshold. The shape of these regions became increasingly oblong with distance from the transducer, as seen in figure 6(c3), where overlays from both empty and full cavity measurements are displayed.

Range in the phantom was estimated from the CT scans as follows: The Styrofoam cone accounted for the equivalent water depth of 4.59 mm = 135 mm * 0.034 and another

0.65 mm = 3 mm * 0.216 in the gelatin-infused cone tip. This left 21.1–5.2 = 15.9 mm/ρ_s penetration into subsequent material. The Bragg peak was therefore expected to occur 15.9 mm = 15.9 mm/0.998 from the air-gelatin interface when the cavity was empty, and 17.5 mm = 15.9 mm/0.911 when the cavity was filled with olive oil. Overlays of the Bragg peak onto the gelatin phantom agree within 1.4 mm, but overestimate the range in non-aerated olive oil by 1.1 mm. In figure 6(c3), reflectors within the olive oil are likely small air bubbles that may have reduced stopping power and increased the range.

Phantom data was collected three hours after water tank data, with exactly the same chopper electronics so the same 61 μs time delay between chopper discharge and proton delivery was utilized for image reconstruction. Because the transducer was more than 3 cm distal to the Bragg peak, first arrivals in phantom data in figures 6(a1) and (b1) have modest curvature compared to the water tank data in figures 5(a)–(c). Optimizing focusing of the Bragg peak with respect to beam delivery time would not have been robust due to the weak curvature of the first arrivals.

5. Discussion

We have presented two synergistic and novel improvements to thermoacoustic range verification: First, proton pulses delivered a therapeutic dose of 2 Gy in less than 2 μs, and generated broadband thermoacoustic emissions. Second, a clinical ultrasound array detected those pulses to create images of the Bragg peak that are perfectly co-registered with ultrasound images that can display the treatment field.

Range estimates appeared to be nearly as accurate from 6 cm distal in a phantom laden with diffuse reflectors than from 6.5 mm distal in a waterbath where acoustic attenuation is negligible. In the waterbath, the Bragg peak was reconstructed as a round shaped monopole, and we underestimated the range by 1.2 mm compared to Monte Carlo simulations. In the empty phantom, reconstructions of the Bragg peak were oblong. When the transducer array was 3 cm distal agreement with range estimates was within 1.2 mm. When the cavity was filled with olive oil, the transducer was 6.5 cm distal and we overestimated the range by 1.4 mm. These results in the gelatin phantom confirm that thermoacoustic range verification is robust to acoustic attenuation because thermoacoustic emissions from pulsed proton therapy beams are low frequency.

Robustness of range estimates from limited aperture clinical transducer arrays will depend more on orientation of the array relative to the Bragg peak rather than distance. This can be understood from two perspectives. Firstly, frequency content is higher when measured from distal locations as modeled by Alsanea *et al* (figure 2), and exploited by Assmann *et al* to detect pulses with MHz frequency content. Secondly, limited angle streak artifacts in reconstructed images run approximately parallel to the transducer surface. Transducer placement distal to the Bragg peak with face perpendicular to the beamline results in streaks artifacts perpendicular to the beamline, which serve to pinpoint the Bragg peak location, as shown by overlays in figure 6. Lateral displacement with transducer face parallel to the beamline would result in streaks running parallel to the beamline, degrading accuracy. We therefore elected a distal transducer location for this benchtop study. Clinical constraints may not always permit distal transducer positioning, forcing one to rely upon separation between the lower-frequency compression and rarefaction peaks measured at lateral transducer displacements (Jones *et al* 2014, 2015).

Thermoacoustic range verification with overlay onto ultrasound images will be robust sound-speed inhomogeneity and modest transducer positioning errors. Soundspeed inhomogeneity

can distort ultrasound images, but thermoacoustic estimates of the Bragg peak location will be similarly distorted, so that the peak will be overlaid onto the correct tissue even if the absolute range estimate is incorrect. Additionally, the series of waterbath images demonstrate robustness to lateral offsets of the transducer position, which is critical for *in vivo* application.

The work we have done to date is preliminary and has limitations. Most notably, we failed to minimize signal averaging for either transducer. Range estimates in the phantom were crudely done and should be improved by a comprehensive stoichiometric conversion of Hounsfield units to proton stopping power (Schneider *et al* 1995) in a more suitable phantom. Following Sulak *et al*, we utilized Styrofoam to translate the Bragg peak deep into the gelatin phantom. However, the exact composition of the cone is unknown, precluding accurate Monte Carlo modeling. Additionally, vertical streaks in the ultrasound images 6a3 and 6c3 indicate that the beam may have damaged the Styrofoam changing the range slightly as we worked. Additionally, a typical clinical dose of 2 Gy was deposited *per pulse,* and 1024 pulses were averaged by the clinical array. Thermoacoustic pulses generated by idealized instantaneous and experimentally realized spills each containing 2e7 protons achieved maximum pressures of 40 Pa and 11 Pa, respectively, as plotted in figure 3(c). Finally, the tightly focused 50 MeV beam was not as energetic as a therapeutic beam and could penetrate only 2 cm in water and phantom material. Higher energy clinical beams typically have larger radius upon entry and experience more range straggle, further spreading the delivered dose which will generate lower frequency thermoacoustic emissions, so validation at clinical beam energies will be critical.

Future directions of research include further reducing proton beam pulsewidth and modifying the injection line to ensure safe delivery of rapid and intense ion pulses, improving sensitivity of a few elements to very low acoustic frequencies, and reconfiguring our setup to enable online adaptive treatment.

Reducing spill time will increase bandwidth and maximum pressure induced, reducing the number of pulses required. Delivering proton pulsewidths of 1 μs should be feasible for LBNL's 88″ cyclotron with relatively minor improvements to the chopper. Similar choppers can be installed in any system with sufficient space for a deflector plate between the ion source and the point at which the beam is accelerated, i.e. before the cyclotron inflector for external ion sources or close to the cyclotron middle region for internal ion sources. Next generation systems utilizing laser driven proton beams will deliver a broad energy spectrum with nanosecond pulse durations, presenting both an opportunity and a challenge. Short proton pulse durations will be ideal for thermoacoustics, but dose will not be concentrated in the Bragg peak. Validating energy selection methods (Masood *et al* 2014) will require quantifying dose along the entire beamline rather than merely identifying the Bragg peak location.

To minimize the risk of overdose, the ion source and chopper should be designed so that the system's default state is no acceleration. Ions should be accelerated only when deflected *towards* the acceleration point. Additionally, a safety interlock on the chopper limiting deflection time would limit the maximum dose delivered per pulse.

Customized ultrasound arrays will be required to generate clinical quality ultrasound images *and* detect thermoacoustic emissions generated by rapid delivery of a 2 Gy therapeutic dose. Diagnostic ultrasound is an established and highly optimized technique utilizing envelope detection, which reduces image resolution to the envelope width. In comparison, half-wavelength resolution can be achieved by backprojecting thermoacoustic emissions. Additionally, frequency of B-mode ultrasound measurements is determined by the center frequency of the transmitted ultrasound pulse, whereas thermoacoustic spectra are low-pass limited by ion pulse duration and beam shape. Therefore, we anticipate maintaining the center frequency of ultrasound imaging channels above 1 MHz and incorporating a few elements

sensitive to frequencies below reciprocal of the ion pulsewidth, e.g. 500 kHz for the current LBNL chopper. The low frequency elements will be dedicated to detecting thermoacoustic emissions, so they may operate in receive-only mode. Matching their frequency response to thermoacoustic emissions will allow us to reduce signal averaging, while leaving the ultrasound image quality unchanged.

Finally, the system should be reconfigured to minimize dose and enable online adaptive treatment. In these experiments, beam was pulsed continuously, even while saving data to disk. Instead, the ultrasound system should trigger both chopper and oscilloscope to which the scintillator is read out. This configuration would enable online treatment management on a spot-by-spot basis. The ultrasound system's host computer could track motion in ultrasound images and trigger beam delivery only when the target was properly positioned, and immediately overlay thermoacoustic emissions to validate that the spot had been properly treated.

6. Conclusions

Thermoacoustic range verification with better than 1.5 mm accuracy in homogeneous targets has been demonstrated with a commercial clinical ultrasound array, but at doses exceeding the clinical realm. Further optimization of both transducer array and injection line chopper will be required to enable online adaptive planning for treating tumors that can be visualized by ultrasound.

Acknowledgments

We thank M Zolotorev and the late A Sessler for introducing us to thermoacoustic range verification and assembling the team. SKP thanks J Shen for providing many primers on proton therapy, F Caspers for enthusiastic advice, L Dong for practical advice, G Noid and X A Li for providing CT scans of the phantom. Finally, constructive criticism of anonymous reviewers greatly strengthened this manuscript.

This work was supported in part by a UWM Intramural Instrumentation Grant and by the Director, Office of Science, Office of Nuclear Physics, of the US Department of Energy under Contract No. DE-AC02-05CH11231. YMQ was supported by a UWM-OUR summer fellowship.

References

Ahmad M, Xiang L, Yousefi S and Xing L 2015 Theoretical detection threshold of the proton-acoustic range verification technique *Med. Phys.* **42** 5735

Albul V I, Bychkov V B, Vasil'ev S S, Gusev K E, Demidov V S, Demidova E V, Krasnov N K, Kurchanov A F, Luk'yashin V E and Sokolov A Y 2005 Acoustic field generated by a beam of protons stopping in a water medium *Acoust. Phys.* **51** 33–7

Alsanea F, Moskvin V and Stantz K M 2015 Feasibility of RACT for 3D dose measurement and range verification in a water phantom *Med. Phys.* **42** 937–46

Assmann W *et al* 2015 Ionoacoustic characterization of the proton Bragg peak with submillimeter accuracy *Med. Phys.* **42** 567–74

ASTRO Payer Relations Subcommittee 2013 American Society for Therapeutic Radiology and Oncology—model policies, proton beam therapy (PBT) *Indications and Limitations of Coverage and/or Medical Necessity—Group 2* (Arlington, VA: ASTRO)

Cambraia Lopes P *et al* 2015 Time-resolved imaging of prompt-gamma rays for proton range verification using a knife-edge slit camera based on digital photon counters *Phys. Med. Biol.* **60** 6063–85

Covo M K 2014 Nondestructive synchronous beam current monitor *Rev. Sci. Instrum.* **85** 125106

Dendooven P, Buitenhuis H J, Diblen F, Heeres P N, Biegun A K, Fiedler F, van Goethem M J, van der Graaf E R and Brandenburg S 2015 Short-lived positron emitters in beam-on PET imaging during proton therapy *Phys. Med. Biol.* **60** 8923–47

Frey K, Unholtz D, Bauer J, Debus J, Min C H, Bortfeld T, Paganetti H and Parodi K 2014 Automation and uncertainty analysis of a method for *in vivo* range verification in particle therapy *Phys. Med. Biol.* **59** 5903–19

Hayakawa Y, Tada J, Arai N, Hosono K, Sato M, Wagai T, Tsuji H and Tsujii H 1995 Acoustic pulse generated in a patient during treatment by pulsed proton radiation beam *Radiat. Oncol. Investig.* **3** 42–5

Hueso-Gonzalez F *et al* 2015 First test of the prompt gamma ray timing method with heterogeneous targets at a clinical proton therapy facility *Phys. Med. Biol.* **60** 6247–72

Hunter S D *et al* 1981 Acoustic signals of nonthermal origin from high energy protons in water *J. Acoust. Soc. Am.* **69** 1557–62

John F 1981 *Partial Differential Equations* 4th edn (New York: Springer) pp 135–6

Johnson M B, McMahan M A, Gimpel T L and Tiffany W S 2006 Berkeley accelerator space effects (BASE) light ion facility upgrade *2006 IEEE Radiation Effects Data Workshop* pp 183–7

Jones K C, Vander Stappen F, Bawiec C R, Janssens G, Lewin P A, Prieels D, Solberg T D, Sehgal C M and Avery S 2015 Experimental observation of acoustic emissions generated by a pulsed proton beam from a hospital-based clinical cyclotron *Med. Phys.* **42** 7090

Jones K C, Witztum A, Sehgal C M and Avery S 2014 Proton beam characterization by proton-induced acoustic emission: simulation studies *Phys. Med. Biol.* **59** 6549–63

Knopf A C and Lomax A 2013 *In vivo* proton range verification: a review *Phys. Med. Biol.* **58** R131–60

Lazebnik M, Madsen E L, Frank G R and Hagness S C 2005 Tissue-mimicking phantom materials for narrowband and ultrawideband microwave applications *Phys. Med. Biol.* **50** 4245–58

Learned J 1979 Acoustic radiation by charged atomic particles in liquids: an analysis *Phys. Rev.* D **19** 3293–307

Madsen E L, Zagzebski J A and Frank G R 1982 Oil-in-gelatin dispersions for use as ultrasonically tissue-mimicking materials *Ultrasound Med. Biol.* **8** 277–87

Masood U, Bussmann M, Cowan T E, Enghardt W, Karsch L, Kroll F, Schramm U and Pawelke J 2014 A compact solution for ion beam therapy with laser accelerated protons *Appl. Phys.* B **117** 41–52

Min C-H, Kim C, Youn M-Y and Kim J-W 2006 Prompt gamma measurements for locating the dose falloff region in the proton therapy *Appl. Phys. Lett.* **89** 183517

Min C H, Lee H R, Kim C H and Lee S B 2012 Development of array-type prompt gamma measurement system for *in vivo* range verification in proton therapy *Med. Phys.* **39** 2100–7

Panofsky W K 1997 Evolution of particle accelerators *SLAC Beam Line* **27** 36–44

Patch S, Hull D, See W and Hanson G 2015 Towards quantitative whole organ thermoacoustics with a clinical array plus one very low frequency channel applied to prostate cancer imaging *IEEE Trans. Ultrason. Ferroelectr. Freq. Control* **63** 245–55

Polf J C, Avery S, Mackin D S and Beddar S 2015 Imaging of prompt gamma rays emitted during delivery of clinical proton beams with a Compton camera: feasibility studies for range verification *Phys. Med. Biol.* **60** 7085–99

Polf J and Parodi K 2015 Imaging particle beams for cancer treatment *Phys. Today* **68** 28–33

Rohrer L, Jakob H, Rudolph K and Skorka S 1984 The 4 gap double drift buncher at Munich *Nucl. Instrum. Methods Phys. Res.* **220** 161–4

Schneider U, Pedroni E and Lomax A 1995 The calibration of CT Hounsfield units for radiotherapy treatment planning *Phys. Med. Biol.* **41** 111–24

Selman J 2000 *The Fundamentals of Imaging Physics and Radiobiology* (Springfield, IL: Charles C Thomas)

Sulak L *et al* 1979 Experimental studies of the acoustic signature of proton beams traversing fluid media *Nucl. Instrum. Methods* **161** 203–17

Tada J, Hayakawa Y, Hosono K and Inada T 1991 Time resolved properties of acoustic pulses generated in water and in soft tissue by pulsed proton beam irradiation—a possibility of doses distribution monitoring in proton radiation therapy *Med. Phys.* **18** 1100–4

Toulemonde M, Surdutovich E and Solov'yov A V 2009 Temperature and pressure spikes in ion-beam cancer therapy *Phys. Rev.* E **80** 031913

Verburg J M, Riley K, Bortfeld T and Seco J 2013 Energy- and time-resolved detection of prompt gamma-rays for proton range verification *Phys. Med. Biol.* **58** L37–49

Ziegler J, Ziegler M and Biersack J 2010 SRIM—the stopping and range of ions in matter *Nucl. Instrum. Methods Phys. Res.* B **268** 1818–23